Unraveling nodal-line semimetallic phase in $SrIrO_3$ by terahertz quasiparticle dynamics

K. Santhosh Kumar,[1] Anagha P.,[1] Canon Sun,[2] and D. S. Rana[1,*]

[1]*Department of Physics, Indian Institute of Science Education and Research Bhopal, Bhopal 462066, India*

[2]*Institute for Quantum Matter and Department of Physics and Astronomy, John Hopkins University, Baltimore, Maryland 21218, USA*

(Received 21 November 2021; revised 12 September 2022; accepted 1 December 2022; published 21 December 2022)

We demonstrate a rare nonsymmorphic crystalline symmetry-protected nodal-line semimetallic phase in $SrIrO_3$ by acquiring a spatial dependence of the terahertz spectral structure. An extremely low momentum-relaxation scattering rate of $\sim$8.32 cm^{-1} emerging from high-mobility Dirac electrons, diversity in the carrier dynamics controlled by the orientation and symmetry of epitaxial thin films, and a group theory analysis corroborate the formation of this phase. The presence of Dirac electrons only along selected crystal orientations of this three-dimensional semimetal uniquely interrelates the symmetry-enforced band crossings, a template that can explore the prevalence of this superior topological phase in complex systems.

DOI: 10.1103/PhysRevB.106.245135

I. INTRODUCTION

Anticipation, experimental verification, and understanding the properties of topologically nontrivial electronic phases have renewed enormous scientific interest in emergent quantum materials. Recent advances in this area are attributed to the realization of high-energy particles and their unique response to external perturbations [1–4]. In Dirac and Weyl semimetals, the momentous difference in low-energy quasiparticle excitations with conventional Schrödinger fermions is the source of ultrahigh carrier mobility and related extraordinary physical properties [5,6]. Unconventional band dispersion, as for Dirac nodes, arises at a point in the Brillouin zone with the simultaneous presence of time-reversal (T) and inversion (P) symmetries. Breaking either of these symmetries splits the fourfold Dirac point into a pair of twofold Weyl points [7]. In the presence of spin-orbit coupling (SOC), however, additional crystalline symmetries are required against the band-gap opening [8]. This is exemplified in Na_3Bi (Cd_3As_2) where the Dirac point is protected by uniaxial rotation symmetry C_3 (C_4) [9]. A Dirac-type band dispersion can also occur along the line in the Brillouin zone resulting in a superior topological formation known as the nodal-line semimetal (NLSM) phase. This is stabilizes with PT and mirror symmetries in the absence of SOC, while it requires a nonsymmorphic symmetry such as glide plane/screw rotation in the presence of SOC [10,11]. Collective theoretical and computation research efforts have successfully envisioned several materials with the NLSM phase. However, experimental demonstrations of this phase are not prevalent, and in fact, rare in complex oxides. Appropriate experimental tools and structural forms of the materials are the limiting factors for the observation of this novel quantum phase.

The 5d transition metal oxides with sizable SOC under the synergistic influence of electron correlations are a promising class of materials to host topological semimetallic phases [12–16]. Iridium oxides, a popular class of perovskites, $AIrO_3$ (A = Sr, Ca) in particular, are predicted to exhibit a very elusive NLSM phase [13,16]. However, an experimental demonstration of this novel topological phase formation is yet to be made. Tight-binding and density functional theory calculations predicted the Dirac NLSM phase in $SrIrO_3$ driven by the $J_{\text{eff}} = 1/2$ states crossing in the U-R-X plane. This band crossing is stabilized by the intricate interplay of electron correlations and SOC, and protected by nonsymmorphic crystalline symmetries [13,16–19]. In general, the signature of a Dirac phase usual manifests in (i) giant and negative linear magnetoresistance, and the planar Hall effect via magnetotransport measurements [5,6,20], (ii) linear frequency dependence and flat bands in optical conductivity [21,22], and (iii) linear electronic bands in angle-resolved photoemission spectroscopy (ARPES) data, etc. [23]. While the ARPES data revealed the presence of a Dirac-like dispersion in $SrIrO_3$ [24], however, this technique could not demonstrate the NLSM phase. Thus, in the search for different strategies to unravel the presence of this phase, we combine terahertz (THz) time-domain spectroscopy (TDS) along the selective crystal-axis and an elaborate group theory analysis to unravel the NLSM in the complex oxide $SrIrO_3$. These investigations were carried out on $SrIrO_3/NdGaO_3$ (001) and $SrIrO_3/NdGaO_3$ (110) epitaxial thin films of thickness $\sim$65 nm; two differently orthorhombic distorted phases allow probing the crystal symmetries conforming to the NLSM phase.

II. RESULTS AND DISCUSSIONS

A. THz time-domain spectroscopy results

Figure 1 shows THz real conductivity and other parameters derived from the fitting to this optical conductivity with the Drude model and its modified version for a $SrIrO_3/NdGaO_3$ (001) thin film along the two in-plane orthogonal crystallographic directions [100] and [010] [25,26]. The crystal

*dsrana@iiserb.in

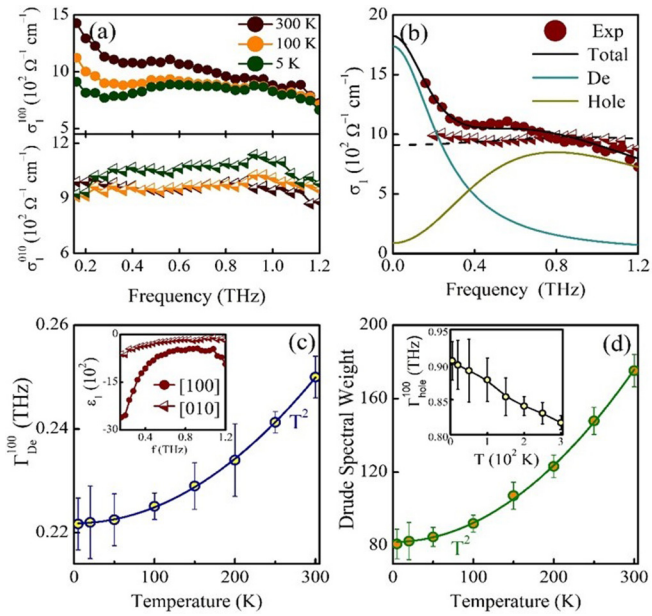

FIG. 1. THz optical properties of a $SrIrO_3/NdGaO_3$ (001) thin film and evidence of Dirac fermions. (a) Temperature-dependent THz conductivity along the [100] (solid circle) and [010] (semisolid triangle) directions. (b) Room-temperature THz conductivity with Drude+Drude-Smith model and Drude-Smith model fittings for the [100] (solid line) and [010] (dotted line) directions, respectively. The scattering rate of Dirac electrons (Γ_{De}^{100}) and the Drude spectral weight as a function of temperature are presented in (c) and (d). The temperature dielectric constant for the [100] and [010] directions, and the scattering rate of holes is given in the insets of (c) and (d), respectively. Here, the optical parameters are denoted as X_y^z [X is the optical parameter, z is the direction ([100] or [010]), and y is the charge carrier type: "De" stands for Dirac electrons and "hole" for holes].

structure of the thin film is estimated to be the monoclinic $P12_1/n1$ or $P2_1/b11$ space group from the reciprocal space mapping results and Glazer notations [see Supplemental Material (SM) [27]]. The real and imaginary conductivities along the [100] and [010] directions are labeled as σ_1^{100} and σ_2^{100}, and σ_1^{010} and σ_2^{010}, respectively. The σ_1^{100} and σ_2^{100} (Fig. S5 [27]) exhibit a unique feature which segregates the conductivity into two different spectral regimes: (i) below 0.4 THz, a sharp increase in THz real conductivity, and (ii) above 0.4 THz, a broad Lorentzian shape of real conductivity [the dielectric constant will be related in the inset of Fig. 1(c)]. These signatures in σ_1^{100} and σ_2^{100} persist down to 5 K. Frequency-dependent conductivity gradually diminishes upon decreasing the temperature, which is consistent with dc electrical resistivity (Figs. S4 and S7 [27]). The conductivity dynamics (σ_1^{100} and σ_1^{010}) along two directions are discernibly different as shown in Fig. 1(a). The former shows a sharp rise below 0.4 THz, while the latter remains flat and nearly frequency independent as shown in Fig. 1(a) [σ_1^{010} and σ_2^{010} (Fig. S5 [27])]. The electronic structure of $SrIrO_3$ contains a Dirac-like feature along with a hole band at the Fermi level [21]. Therefore, the optical conductivities σ_1^{100} and σ_2^{100} were evaluated in the framework of a two-band model (Drude+Drude-Smith model), and the featureless σ_1^{010} and σ_2^{010} were modeled only in a single-band picture (Drude-Smith model) (see SM [27]). Here, we have assigned the Drude model for Dirac electrons and the Drude-Smith model for hole carriers.

The Drude mode (narrow) is confined to the low THz regime while the broad Drude-Smith mode extends to high frequencies along the [100] direction [Fig. 1(b)]. Thus the obtained scattering rate (momentum relaxing) for a narrow Drude mode ($\Gamma_{De}^{100} = 1/\tau_d$, where De stands for the Dirac electron) is 0.25 THz (8.32 cm^{-1}) at 300 K, which is extremely low compared to that of conventional metals (more than 10 THz). As per the mobility ($\mu = e\tau/m$), such a slow relaxation is possible either in heavy fermions or high-mobility electron systems. However, the heavy-fermion behavior is clearly discarded in $SrIrO_3$ as it is predicted to be a topological semimetal. Despite the average value of the carrier effective mass in $SrIrO_3$, a high mobility up to $\sim$1000 $cm^2\,V^{-1}\,s^{-1}$ was reported and this mobility greatly depends on the thin-film quality [28,29]. In addition, a large mobility up to $\sim$60 000 $cm^2\,V^{-1}\,s^{-1}$ was reported in its sister compound $CaIrO_3$ [18]. Hence, the low scattering rate of the narrow Drude mode can be attributed to the intraband excitations of the high-mobility Dirac electrons. Furthermore, the T^2 dependence of Γ_{De}^{100}, as shown in Fig. 1(c), corroborates the Fermi-liquid-like behavior of Dirac electrons in the [100] direction. However, it is not unique to topological materials. The room-temperature Γ_{De}^{100} corresponds to a relaxation time of $\tau_{De}^{100} = 1/(2\pi c\Gamma_{De}^{100}) = 0.63$ ps. Therefore, the upper and lower boundaries of the momentum relaxation length ($l_{De}^{100} = v_F \times \tau_{De}$) are 0.32 μm and 76.3 nm for $v_F = 5.0 \times 10^5$ m/s and 1.2×10^5 m/s, respectively [30]. The l_{De}^{100} increases as large as 0.36 μm and 86 nm at 5 K, respectively. Generally, for a semimetal with dispersion $E \sim |k|^z$, the temperature-dependent Drude weight is defined as $\omega_p^2 \sim T^{(1+1/z)}$ [31]. In the present case, the Drude spectral weight calculated using Eq. (1) given below follows T^2 dependence. Here, $z = 1$ indicates a linear dispersion of bands that contributes to the narrow Drude mode. The vanishing of spectral weight towards low temperatures indicates a strong temperature dependence of the chemical potential with a semimetallic nature, whereas this feature is constant for conventional metals [32]. The optical features as elaborated above are similar to those of a Dirac semimetal, which suggests $SrIrO_3$ to be a Dirac liquid,

$$SW_{\text{Drude}} = \int_0^\infty \sigma_1(\omega)d\omega = \frac{\pi^2}{Z_0}\omega_p^2, \tag{1}$$

where Z_0 is the impedance of free space.

The scattering rate obtained for the hole band ($\Gamma_{\text{hole}}^{100}$) in the [100] direction is given in Fig. 1(d). The $\Gamma_{\text{hole}}^{100}$ increases at low temperature, which suggests a semiconducting behavior and is exemplified by dc resistivity (Fig. S4 [27]). However, the scattering rate ($\Gamma_{\text{hole}}^{010}$) of a single hole band in the [010] direction increases linearly with increasing temperature. Overall, these optical conductivity results confirm the presence of Dirac electrons in the [100] direction while the same is absent in the [010] direction. Now the following question arises: Is the Dirac feature confined only to the a axis? To answer this, we performed in-plane angle-dependent THz spectroscopy measurements on a $SrIrO_3/NdGaO_3$ (001) thin film. The angle-dependent conductivity (σ_1) and dielectric constant (ε_1)

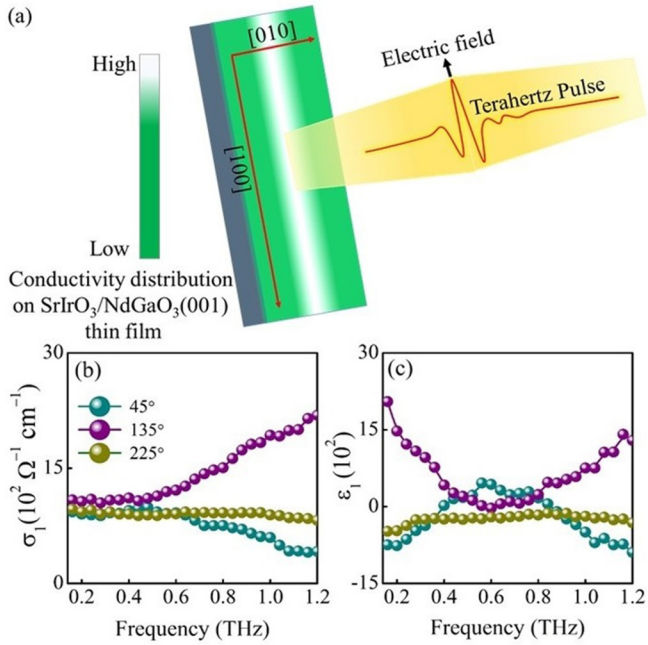

FIG. 2. Unidirectional confinement of Dirac electrons in the in plane of a $SrIrO_3/NdGaO_3$ (001) thin film. (a) shows a schematic of the angle-dependent THz optical properties of the $SrIrO_3/NdGaO_3$ (001) thin film at room temperature. (b) and (c) represent the conductivity (σ_1) and dielectric constant (ε_1) at 45°, 135°, and 225°, respectively.

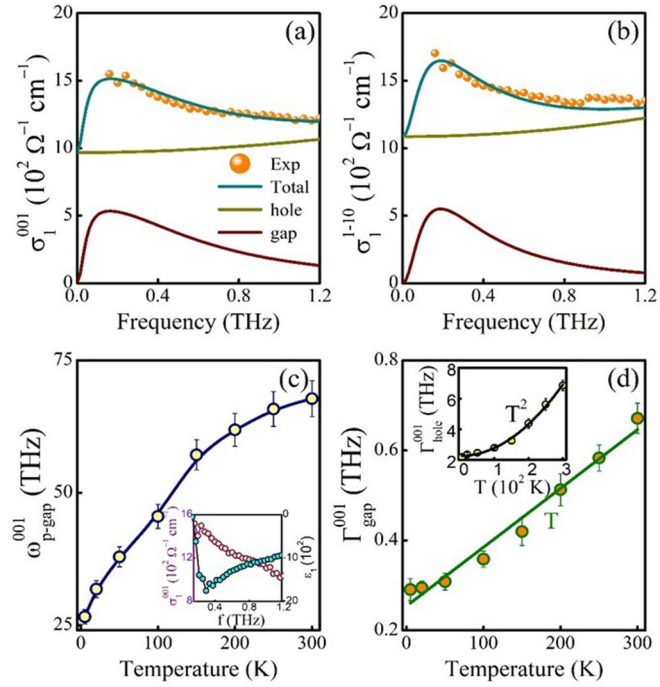

FIG. 3. Gapped topological phase in a $SrIrO_3/NdGaO_3$ (110) thin film. (a) and (b) Room-temperature THz conductivity along the two orthogonal in-plane directions (001) and (1$\bar{1}$0) with Lorentz+Drude-Smith model fittings, respectively. The optical parameters of the Lorentz mode ($\omega^{001}_{p-\mathrm{gap}}$ and $\Gamma^{001}_{\mathrm{gap}}$) as a function of temperature in the (001) direction are given in (c) and (d). The dielectric dispersion and scattering rate ($\Gamma^{001}_{\mathrm{hole}}$) of holes in the (001) direction are given in the insets of (c) and (d), respectively.

in the *ab* plane [in plane of a $NdGaO_3$ (001) substrate] at 45°, 135°, and 225° are plotted in Fig. 2. These data reveal that a sharp rise in σ_1^{100} at low frequencies followed by high negative values of ε_1^{100} as observed previously at 0° (along the *a* axis of the $NdGaO_3$ substrate) disappears at 45°, 135°, and 225°. This confirms that the Dirac-like feature is absent along all other directions in the *ab* plane except along the *a* axis.

To further corroborate the presence of the Dirac NLSM phase in $SrIrO_3$, we have performed the same set of measurements on a $SrIrO_3/NdGaO_3$ (110) thin film with monoclinic $P112_1/m$ crystal symmetry. Room-temperature σ_1^{001} (σ_2^{001} shown in Fig. S6 [27]) along the [001] direction is shown in Fig. 3(a). A striking feature is an optical excitationlike mode superimposed on a broad Drude-Smith-type conductivity spectrum. The low-frequency dielectric dispersion [inset of Fig. 3(c)] suggests an optical excitation mode. The complex conductivity ($\sigma_1^{1\bar{1}0}$ [Fig. 3(b)] and $\sigma_2^{1\bar{1}0}$ (shown in Fig. S6 [27])) along the [1$\bar{1}$0] direction follows a similar trend as in the [001] direction except for a dominant negative imaginary conductivity due to a broad Drude-Smith mode contribution. These features of σ_1^{001} and $\sigma_1^{1\bar{1}0}$ (Fig. S6 [27]) are consistent down to 5 K, except for a slight change in spectral weight. A close observation indicates a slight increase in σ_1^{001} up to 150 K, which decreases towards low temperatures. This is consistent with the metal-insulator transition in dc electrical resistivity (Figs. S4 and S7 [27]). The temperature-dependent conductivity dynamics in the [1$\bar{1}$0] direction also exhibit a trend similar to that along the [001] direction. This complex conductivity was modeled using the Lorentz+Drude-Smith model [25,33] (see SM [27]) to obtain insights into the conductivity dynamics.

An optical energy gap (Δ^{001}) of ∼0.19 THz (6.33 cm^{-1}) was observed at 5 K in the [001] direction. This gap shows a subtle decrease as the temperature increases. The $\omega^{001}_{p-\mathrm{gap}}$ shows a minimum of 26.59 THz at 5 K and it increases drastically with increasing temperature, and finally saturates at 300 K. This emphasizes the role of thermally excited carriers contributing to the Lorentz mode due to a low-energy gap (Δ^{001}) which is well below the room-temperature thermal energy (∼25 meV). The linewidth of the Lorentz mode ($\Gamma^{001}_{\mathrm{gap}}$) increases linearly with temperature, suggesting a thermal broadening of the mode. A $\Gamma^{001}_{\mathrm{hole}}$ of the hole band, however, exhibits a quadratic temperature dependence. This sign of $\Gamma^{001}_{\mathrm{hole}}$ is consistent with the expected behavior of a Fermi liquid. The $\Gamma^{100}_{\mathrm{hole}}$, $\Gamma^{001}_{\mathrm{hole}}$ and the dc transport along [100] and [001] also confirm that the dc electrical resistivity is mainly dominated by the hole band. Further, the obtained optical parameters along the [1$\bar{1}$0] direction follow a trend similar to that along [001], except for a slight change in the magnitude. The Δ^{1-10} is ∼0.22 THz (7.33 cm^{-1}) at 5 K, which is slightly higher than Δ^{001} (6.33 cm^{-1}).

B. Group theory analysis and discussions

Thus the presented experimental results and their interpretations were corroborated by elaborate group theory analysis

as follows. Consider a spin-1/2 $SrIrO_3$ system with *Pbnm* space group and time-reversal symmetry (T) in the presence of SOC. We focus on the $k_b = \pi$ plane which is invariant under the n-glide plane (G_n) operation. The eigenvalues of the n-glide plane $n_\pm = \pm ie^{i(k_a+k_c)/2}$ serve as good quantum numbers to represent the Bloch states on the entire $k_b = \pi$ plane. The composite symmetry Θ is defined as $P * T$ (P is inversion symmetry). $\Theta^2 = -1$ ensures a twofold degeneracy of the Kramers pair in the entire momentum space. At the U point $(0, \pi, \pi)$, the Bloch states are invariant under the twofold screw S_a (eigenvalues are $a_\pm$) operation, in addition to G_n. Thus there exist two complete sets of eigenstates at the U point $|n_+, a_+\rangle$, $|n_+, a_-\rangle$, $\Theta|n_+, a_+\rangle$, $\Theta|n_+, a_-\rangle$ and $|n_-, a_+\rangle$, $|n_-, a_-\rangle$, $\Theta|n_-, a_+\rangle$, $\Theta|n_-, a_-\rangle$ under the b-glide operation (G_b). As the bands evolve from the time-reversal invariant momentum U point to any point on the R-S line, the anticommutation relation $\{G_n, G_b\} = 0$ maps the n_+ state into the n_- state. This enforces the band crossing somewhere between the U point to any point on the R-S line. The band crossing is symmetry protected with the doubly degenerate bands with both opposite G_n and S_a eigenvalues. Similarly, the symmetry-enforced band crossing exists along the path from the U point to any point on the X-S line under the anticommutation $\{G_n, S_a\} = 0$. This suggests the presence of a symmetry-protected fourfold Dirac nodal ring on the $k_b = \pi$ plane with the U point as the center in $SrIrO_3$ [11,19] (detailed calculations are given in the SM [27]).

In the following section, we discuss the nodal line upon breaking the selective spatial symmetries. The *Pbnm* space group is broken down into three different subgroups with T preserved: (I) $P12_1/n1$, (II) $P2_1/b11$, and (III) $P112_1/m$. By symmetry analysis, we find the nodal line in these cases to be (I) preserved, (II) gapped except at isolated Dirac points, and (III) fully gapped.

Case (I): Dirac nodal-line semimetallic phase, $P12_1/n1$. This space group is generated by P and G_n. The S_a and G_b are no longer symmetry operations, hence, the fourfold crossing on the $k_b = \pi$ plane is lifted. Therefore, the nodal line is no longer enforced by symmetry. Nevertheless, the nodal-line crossing persists because, as discussed above, it is a crossing between the bands with opposite n-glide eigenvalues which remains a good quantum number in the lower-symmetry phase. The hybridization between these bands is forbidden without breaking the n-glide symmetry (Fig. 4).

Case (II): Dirac nodal point semimetallic phase, $P2_1/b11$. This space group is generated by P and S_a. As G_n is broken, the nodal line is generally gapped unless it is protected by residual symmetries. There are two such conditions: the crossing on the U-R line whose momentum is invariant under S_a, and on the U-X line that is left invariant by $G_b = S_aP$. The Bloch states along the U-R line can be labeled simultaneously by their G_n and S_a eigenvalues due to the commutation relation $[G_n, S_a] = 0$. Moreover, the Kramers partners have the same G_n and S_a eigenvalues. At point U (R), the operation G_b relates the states with the same (opposite) G_n eigenvalue but opposite (same) S_a eigenvalue. This enforces the pair switching between doubly degenerate bands with opposite G_n and S_a eigenvalues in the symmetry-unbroken phase along the U-R line. As a result, the band crossing perseveres due to the inherited S_a eigenvalues in the lower-symmetry state.

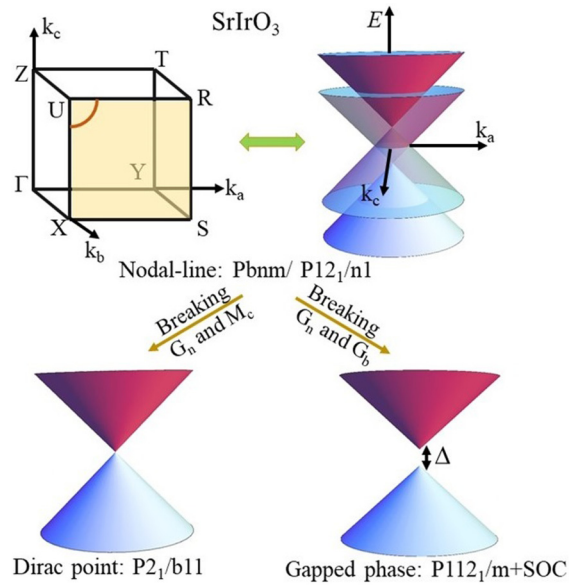

FIG. 4. Topological phase transition of the nodal line upon crystal symmetry breaking in $SrIrO_3$. Schematic diagram of the Brillouin zone of the orthorhombic $SrIrO_3$ unit cell with a nodal ring at the U point, and a Dirac point node and gapped phase upon breaking the selective crystal symmetry.

The crossing along the U-X line, in contrast, is not protected by G_b. This is because the Kramers partners have opposite G_b eigenvalues with $b_\pm = \pm 1$. Thus the doubly degenerate band crossing can in general hybridize. In this phase, therefore, the nodal line turns into two isolated point nodes along the U-R line (Fig. 4). A similar result was observed for the superlattice structure of Sr_2IrRhO_6 where breaking the c-axis mirror symmetry inherently removes the n-glide symmetry and preserves only the b-glide plane. This lifts the nodal-line degeneracy except at the point nodes along the U-R line [17]. This is consistent with the observed high-mobility Dirac electrons in a $SrIrO_3/NdGaO_3$ (001) thin film. We corroborate the electronic ground state of the $SrIrO_3/NdGaO_3$ (001) thin film as a Dirac point node based on THz optical and x-ray diffraction results (see SM [27]). This is also consistent with a previous report on low-symmetry $SrIrO_3$ thin films [34].

Case (III): Gapped phase, $P112_1/m$. This space group is generated by P and the mirror operation M_c. As with the previous case, as G_n is broken, the nodal line is generally gapped with possible exceptions under residual symmetries. Those are the crossing on the U-R line invariant under M_c, and on the U-X line invariant under a twofold screw rotation operation $S_c \equiv M_cP$. The symmetry M_c is unable to protect the crossing on the U-R line: In the *Pbnm* phase, since $M_c = \{1| -1, 0, 1\}S_aG_n$, the pair of states $|n_+a_+\rangle$ and $|n_-a_-\rangle$, and $|n_+a_-\rangle$ and $|n_-a_+\rangle$ have the same M_c eigenvalue. The band crossing enforced by symmetry is between the doubly degenerate bands with opposite G_n and S_a eigenvalues, and the same M_c eigenvalue. In this lower-symmetry phase, though the eigenvalues $n_\pm$ and $a_\pm$ are no longer defined, the M_c eigenvalues remain well defined and unchanged. As the crossing between the same M_c eigenvalue states, the bands are allowed to hybridize and anticross. Further, the crossing

along the U-X line is no longer protected. This is due to the opposite S_c eigenvalues of Kramers partners. As a result, the nodal line is completely gapped in this low-symmetry phase (Fig. 4). This is consistent with the observed optical gap for the $SrIrO_3/NdGaO_3$ (110) thin film. We corroborate the electronic ground state of the $SrIrO_3/NdGaO_3$ (110) thin film as a gapped phase based on THz optical (Fig. 3) and x-ray diffraction results (see SM [27]). This is consistent with the energy gap of ∼5 meV in the Dirac node for the same crystal symmetry of $SrIrO_3$ as predicted by density functional theory calculations [34].

The THz conductivity dynamics reveal the Dirac point node phase of $SrIrO_3/NdGaO_3$ (001) and the gapped phase of $SrIrO_3/NdGaO_3$ (110) thin films. The two-band contribution in the optical conductivity is consistent with the observation of multiple narrow bands in ARPES studies [24]. The finite intraband conductivity originating from linear bands and a small optical gap ($\sim 2\Delta + 2E_F$) from the above results indicate the Dirac band crossing is below and close to the Fermi level. The spatial- and angle-dependent THz data along all crystallographic axes reveal that the Dirac electrons are confined to the real-space a-c plane (i.e., [100] and [001] directions). To summarize, the optical response of thin films as corroborated by group theory analysis suggests a fourfold degenerate Dirac nodal line in $SrIrO_3$ ($Pbnm$ space group) with $J_{\text{eff}} = 1/2$ states. Also, highly anisotropic THz conductivity dynamics and Drude weights confirm the anisotropic nature of the Fermi surface in $SrIrO_3$. This study further suggests that the nonsymmorphic crystalline symmetry-protected nodal-line phase in $SrIrO_3$ is sensitive to epitaxial strain, and exhibits a topological phase transition to a Dirac point and gapped phase upon breaking selective symmetries in the thin-film form.

III. SUMMARY

Thus the demonstrated experimental framework unveils the NLSM phase and its complete topological phase transition in complex oxide $SrIrO_3$. Without THz spectroscopy, the observation of a Dirac electron gas in $SrIrO_3$ is challenging due to an extremely low momentum-relaxation scattering rate (∼400 GHz) and the dominant magnitude of the hole-band conductivity. Further, the observation of an optical gap and evidence of the presence of Dirac electrons along the selected crystal orientations help in understanding the symmetry-enforced band crossings in topological materials. To sum up, THz quasiparticle dynamics unravel a much anticipated NLSM phase in $SrIrO_3$. This will hopefully inspire a different direction of investigations in topological semimetals.

ACKNOWLEDGMENTS

D.S.R. acknowledges the financial support from Science and Engineering Research Board (SERB), New Delhi under Project No. CRG/2020/002338.

[1] Y. L. Chen, J. G. Analytis, J.-H. Chu, Z. K. Liu, S.-K. Mo, X. L. Qi, H. J. Zhang, D. H. Lu, X. Dai, Z. Fang, S. C. Zhang, I. R. Fisher, Z. Hussain, and Z.-X. Shen, Science **325**, 178 (2009).
[2] Z. K. Liu, B. Zhou, Y. Zhang, Z. J. Wang, H. M. Weng, D. Prabhakaran, S.-K. Mo, Z. X. Shen, Z. Fang, X. Dai, Z. Hussain, and Y. L. Chen, Science **343**, 864 (2014).
[3] Z. K. Liu, J. Jiang, B. Zhou, Z. J. Wang, Y. Zhang, H. M. Weng, D. Prabhakaran, S-K. Mo, H. Peng, P. Dudin, T. Kim, M. Hoesch, Z. Fang, X. Dai, Z. X. Shen, D. L. Feng, Z. Hussain, and Y. L. Chen, Nat. Mater. **13**, 677 (2014).
[4] A. A. Burkov, Nat. Mater. **15**, 1145 (2016).
[5] T. Liang, Q. Gibson, M. N. Ali, M. Liu, R. J. Cava, and N. P. Ong, Nat. Mater. **14**, 280 (2014).
[6] C. Shekhar, A. K. Nayak, Y. Sun, M. Schmidt, M. Nicklas, I. Leermakers, U. Zeitler, Y. Skourski, J. Wosnitza, Z. Liu, Y. Chen, W. Schnelle, H. Borrmann, Y. Grin, C. Felser, and B. Yan, Nat. Phys. **11**, 645 (2015).
[7] N. P. Armitage, E. J. Mele, and A. Vishwanath, Rev. Mod. Phys. **90**, 015001 (2018).
[8] B.-J. Yang, T. A. Bojesen, T. Morimoto, and A. Furusaki, Phys. Rev. B **95**, 075135 (2017).
[9] B.-J. Yang and N. Nagaosa, Nat. Commun. **5**, 4898 (2014).
[10] S.-Y. Yang, H. Yang, E. Derunova, S. S. P. Parkin, B.-H. Yan, and M. N. Ali, Adv. Phys. X **3**, 1414631 (2018).
[11] C. Fang, Y. Chen, H.-Y. Kee, and L. Fu, Phys. Rev. B **92**, 081201(R) (2015).
[12] W. Witczak-Krempa, G. Chen, Y. B. Kim, and L. Balents, Annu. Rev. Condens. Matter Phys. **5**, 57 (2014).
[13] M. A. Zeb and H.-Y. Kee, Phys. Rev. B **86**, 085149 (2012).
[14] Y. Sun, Y. Zhang, C.-X. Liu, C. Felser, and B. Yan, Phys. Rev. B **95**, 235104 (2017).
[15] S. Bhowal and S. Satpathy, Phys. Rev. B **100**, 115101 (2019).
[16] Y. Chen, Y.-M. Lu, and H.-Y. Kee, Nat. Commun. **6**, 6593 (2015).
[17] J.-M. Carter, V. V. Shankar, M. A. Zeb, and H.-Y. Kee, Phys. Rev. B **85**, 115105 (2012).
[18] J. Fujioka, R. Yamada, M. Kawamura, S. Sakai, M. Hirayama, R. Arita, T. Okawa, D. Hashizume, M. Hoshino, and Y. Tokura, Nat. Commun. **10**, 362 (2019).
[19] Y. Chen, H.-S. Kim, and H.-Y. Kee, Phys. Rev. B **93**, 155140 (2016).
[20] J. Hu, S.-Y. Xu, N. Ni, and Z. Mao, Annu. Rev. Mater. Res. **49**, 207 (2019).
[21] A. V. Pronin and M. Dressel, Phys. Status Solidi B **258**, 2000027 (2021).
[22] M. B. Schilling, L. M. Schoop, B. V. Lotsch, M. Dressel, and A. V. Pronin, Phys. Rev. Lett. **119**, 187401 (2017).
[23] B. Lv, T. Qian, and H. Ding, Nat. Rev. Phys. **1**, 609 (2019).
[24] Y. F. Nie, P. D. C. King, C. H. Kim, M. Uchida, H. I. Wei, B. D. Faeth, J. P. Ruf, J. P. C. Ruff, L. Xie, X. Pan, C. J. Fennie, D. G. Schlom, and K. M. Shen, Phys. Rev. Lett. **114**, 016401 (2015).
[25] N. V. Smith, Phys. Rev. B **64**, 155106 (2001).
[26] K. Santhosh Kumar, E. V. Phanindra, and D. S. Rana, Phys. Rev. B **100**, 125127 (2019).
[27] See Supplemental Material at http://link.aps.org/supplemental/10.1103/PhysRevB.106.245135 for sample preparation,

structural characterization, temperature dependent THz conductivity along with complex conductivity models that we have used for fitting, and detailed group theory analysis for orthorhombic Pbnm symmetry.

[28] L. Zhang, Q. Liang, Y. Xiong, B. Zhang, L. Gao, H. Li, Y. B. Chen, J. Zhou, S.-T. Zhang, Z.-B. Gu, S.-h. Yao, Z. Wang, Y. Lin, and Y.-F. Chen, Phys. Rev. B **91**, 035110 (2015).

[29] M. Masuko, J. Fujioka, M. Nakamura, M. Kawasaki, and Y. Tokura, APL Mater. **7**, 081115 (2019).

[30] A. Yamasaki, H. Fujiwara, S. Tachibana, D. Iwasaki, Y. Higashino, C. Yoshimi, K. Nakagawa, Y. Nakatani, K. Yamagami, H. Aratani, O. Kirilmaz, M. Sing, R. Claessen, H. Watanabe, T. Shirakawa, S. Yunoki, A. Naitoh, K. Takase, J. Matsuno, H. Takagi *et al.*, Phys. Rev. B **94**, 115103 (2016).

[31] A. B. Sushkov, J. B. Hofmann, G. S. Jenkins, J. Ishikawa, S. Nakatsuji, S. Das Sarma, and H. D. Drew, Phys. Rev. B **92**, 241108(R) (2015).

[32] C. J. Tabert, J. P. Carbotte, and E. J. Nicol, Phys. Rev. B **93**, 085426 (2016).

[33] S. Das, G. L. Prajapati, P. Anagha, and D. S. Rana, Phys. Rev. B **98**, 115110 (2018).

[34] J. Liu, D. Kriegner, L. Horak, D. Puggioni, C. Rayan Serrao, R. Chen, D. Yi, C. Frontera, V. Holy, A. Vishwanath, J. M. Rondinelli, X. Marti, and R. Ramesh, Phys. Rev. B **93**, 085118 (2016).